Journal Pre-proofs

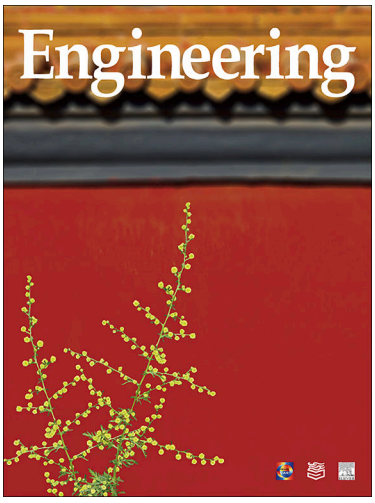

Article

Flexible, All-Polyimide Sensing Skin for Cryogenic Engineering

Lang Yin, Fan Zhang, Jiayang Li, Dawei Liu, Huamin Yu, Shuchuan Li, Huinan Zhang, Yaning Zheng, Zhangyu Xu, Mengfei Yin, Xuejun Liu, Hanqing Liu, Yuxin Guo, Jingjing Ji, Peng Qiao, Guoshuai Li, YongAn Huang

PII: S2095-8099(26)00260-2
DOI: https://doi.org/10.1016/j.eng.2026.04.016
Reference: ENG 2337

To appear in: *Engineering*

Received Date: 9 December 2025
Revised Date: 3 April 2026
Accepted Date: 14 April 2026

Please cite this article as: L. Yin, F. Zhang, J. Li, D. Liu, H. Yu, S. Li, H. Zhang, Y. Zheng, Z. Xu, M. Yin, X. Liu, H. Liu, Y. Guo, J. Ji, P. Qiao, G. Li, Y. Huang, Flexible, All-Polyimide Sensing Skin for Cryogenic Engineering, *Engineering* (2026), doi: https://doi.org/10.1016/j.eng.2026.04.016

Research

Frontiers of Extreme Manufacturing—Article

Flexible, All-Polyimide Sensing Skin for Cryogenic Engineering

Lang Yin [a,b,c], Fan Zhang [a,b,c,*], Jiayang Li [a,b,c], Dawei Liu [d], Huamin Yu [a,b,c], Shuchuan Li [a,b,c], Huinan Zhang [a,b,c], Yaning Zheng [a,b,c], Zhangyu Xu [a,b,c], Mengfei Yin [a,b,c], Xuejun Liu [a,b,c], Hanqing Liu [a,b,c], Yuxin Guo [a,b,c], Jingjing Ji [a,b,c], Peng Qiao [d], Guoshuai Li [d,*], YongAn Huang [a,b,c,*]

[a] *State Key Laboratory of Intelligent Manufacturing Equipment and Technology, Huazhong University of Science and Technology, Wuhan 430074, China*

[b] *Research Center for Advanced Electronics Manufacturing, School of Mechanical Science and Engineering, Huazhong University of Science and Technology, Wuhan 430074, China*

[c] *Flexible Electronics Research Center, Huazhong University of Science and Technology, Wuhan 430074, China*

[d] *High Speed of Aerodynamics Institute, China Aerodynamics Research and Development Center, Mianyang 621000, China*

* Corresponding authors.

E-mail addresses: fanzhang@hust.edu.cn (F. Zhang), gli221132@126.com (G. Li), yahuang@hust.edu.cn (Y.A. Huang).

Abstract: Reliable pressure measurement represents a cornerstone of cryogenic engineering, spanning fields from superconducting magnets and deep-space exploration to cryogenic wind tunnels. However, acquiring accurate *in situ* data in these extreme low-temperature environments remains a formidable challenge, as conventional sensors typically face material embrittlement, seal failure, and performance degradation. Herein, an all-polyimide (PI) intelligent flexible sensing skin (iFlexSense) tailored for pressure monitoring under extreme environmental conditions was proposed. A novel droplet-encapsulation architecture was designed to enhance sensor sensitivity in the high-pressure working range while preserving its response characteristics in the low-pressure working range. This architecture was implemented via a PI electrospray approach, which also ensured robust interlayer adhesion, thereby maintaining structural and hermetic integrity at temperatures down to −196 °C. Additionally, this flexible skin was successfully validated in cryogenic wind tunnels across a broad operational envelope (T_0 = 110–300 K, P_0 = 115–450 kPa, Ma = 0.6–1.3, where T_0 is the total temperature, P0 is the total pressure, and Ma is the Mach number). Results demonstrated excellent fidelity with data from a standard pressure scanner. The sensing skin effectively captured nuanced aerodynamic phenomena, including Reynolds number effects and shock wave evolution. Collectively, the present work establishes the iFlexSense as a robust, versatile tool for high-fidelity pressure mapping in demanding cryogenic engineering applications.

Keywords: Flexible electronics; Cryogenic wind tunnel; Pressure sensing skin; Aerodynamic measurement; Cryogenic engineering

1. Introduction

Cryogenic engineering, broadly defined as the thermal regime below 120 K [1], holds considerable significance in diverse fields, including aircraft aerodynamic testing (e.g., cryogenic wind tunnels, 110 K [2]), space exploration (e.g., Moon, 90 K [3]), and superconducting electronics (e.g., mercury, 4.2 K [4]). In wind tunnel testing, the reduced characteristic length L of the model results in a test Reynolds number (Re) that is one to two orders of magnitude lower than that experienced in actual flight. This "Reynolds number effect," as illustrated in Fig. 1(a), profoundly influences boundary layer development, laminar-turbulent transition, and flow separation [5]. Such modifications may induce structural alterations in complex phenomena like shock-boundary layer interactions, thereby compromising the accuracy of critical aerodynamic metrics such as stall characteristics, friction drag, and shock dynamics [6–8]. With intensifying demand for high-Re ground testing for next-generation aircraft, the global aerospace community has invested heavily in advancing cryogenic wind tunnels [2], including Germany's Kölner Kryo-Kanal (KKK), the USA's National Transonic Facility (NTF), and the European Transonic Windtunnel (ETW) [9]. These tunnels operate under challenging conditions featuring wide total pressure ranges (115–450 kPa) and extremely low, variable temperatures (110–323 K), presenting substantial difficulties for precision measurement instrumentation [10].

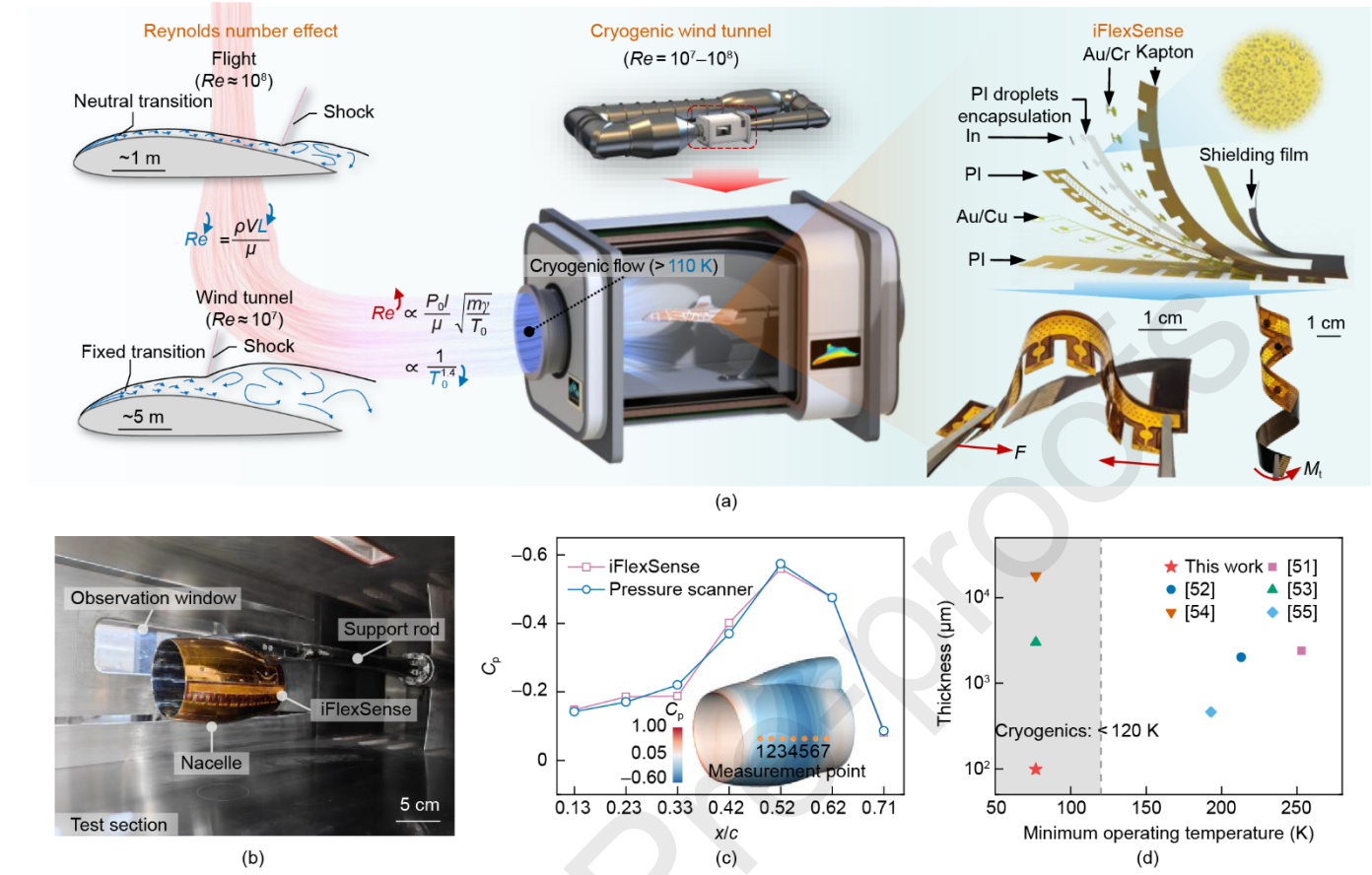

Fig. 1. Architecture of the iFlexSense applied in cryogenic wind tunnels. (a) Schematic of the cryogenic wind tunnel principle, where high-Reynolds-number flight environments are simulated by reducing temperature T_0, and the principle of iFlexSense with mechanical flexibility for static pressure sensing in cryogenic wind tunnels. P_0: total pressure; l: model characteristic length; L: full-scale flight characteristic length; ρ: gas density; V: flow velocity; μ: dynamic viscosity; m: model mass; γ: ratio of specific heats; F: aerodynamic force; M_t: test section Mach number. (b–d) In the 0.3 m cryogenic wind tunnel: (b) Photograph of the iFlexSense mounted on the nacelle model surface. (c) Comparison of pressure coefficient (C_p) distributions measured by iFlexSense and a commercial pressure scanner in 0.3 m cryogenic wind tunnels, together with the reconstruction of the surface pressure distribution. x/c denotes the chordwise position of the measurement points. (d) Benchmarking of representative flexible low-temperature pressure sensors in terms of minimum operating temperature and device thickness. The shaded region marks the cryogenic regime (< 120 K).

Conventional surface pressure measurement techniques in cryogenic environments include silicon-based sensors [11], pressure taps [12], and cryogenic pressure-sensitive paint (PSP) [13]. Both silicon sensors and pressure taps are intrusive by nature. Their integration must be determined during the model's design phase and inherently compromises the model's structural integrity—most commonly by requiring holes to be drilled into the surface. On the other hand, PSP, an optical technique, still faces challenges in terms of accuracy, signal-to-noise ratio, and occluded regions.

Flexible electronics [14–17], offering conformal [18–20], *in situ* [21–23], and large-scale [24–26] measurement capabilities, have emerged as a promising alternative. They can be employed to quantify fundamental flow parameters (pressure [27,28] and shear stress [29,30]), identify complex flow features (transition and separation [31,32]), and estimate flight attitudes [33,34]. However, existing flexible pressure sensors are typically designed for ambient conditions and remain challenging in cryogenic environments [35] due to the following critical challenges:

(1) With decreasing temperature, the sensitivity of flexible sensors degrades significantly, eventually leading to complete functional failure. Existing sensitivity-enhancement strategies such as microstructures [36–39] become ineffective. At low temperatures, the flexible and deformable nature of these microstructured elastomer is compromised by factors like the glass transition [40], rendering them brittle and failing [41]. Furthermore, research on elastomeric materials capable of stable operation in cryogenic environments [42,43] is still limited. Another typical design for high-sensitivity, wide-range sensors—

ionic capacitive pressure sensors [44–46]—also remains challenging under cryogenic conditions, as the solvents or ion pairs within them tend to crystallize at low temperatures.

(2) There are irreversible damages to interfacial adhesion [47]. Reliably sealed interlayer interfaces matter considerably for gaseous pressure measurement. However, adhesives suitable for deep cryogenic applications have been rarely reported [48]. Additionally, the mismatch in the coefficient of thermal expansion (CTE) between the adhesive and the flexible sensor substrate presents a significant and unresolved challenge [49].

Herein, an all-polyimide (PI) intelligent flexible sensing skin (iFlexSense) was developed for pressure sensing in cryogenics, where the substrate, encapsulation, and adhesive layers were all PI-based. PI was selected for its exceptional mechanical compliance at cryogenic temperatures, which prevented it from becoming hard and brittle [50]. A novel droplet-encapsulation architecture for capacitive pressure-sensing elements was accordingly developed using the PI electrospray approach. This design permitted continued electrode deformation into the interstitial voids, thus exhibiting enhanced sensitivity in the high-pressure working range—a critical feature for cryogenic wind tunnels—compared to dense encapsulated sensors. Furthermore, this integrated electrospray approach also yielded a robust interlayer bonding mechanism, allowing the flexible skin to operate at cryogenic temperature. The conformability and fidelity of iFlexSense (Fig. 1(b)) were successfully validated in cryogenic wind tunnels. Leveraging data assimilation algorithms, the sensor system enabled the reconstruction of high-precision, full-field pressure distributions, visually capturing complex aerodynamic features (Fig. 1(c)). To place iFlexSense in context for cryogenic wind-tunnel pressure mapping, representative cryogenic pressure instrumentation and representative flexible low-temperature pressure sensors were hereby summarized, as shown in Table S1 in Appendix A. Compared with state-of-the-art low-temperature flexible pressure sensors [51–55] reported in recent years (Fig. 1(d)), this work not only uniquely offers air pressure measurement capabilities, but also delivers optimal performance in both minimum operating temperature (–196 °C, i.e., 77 K) and thickness (98.4 μm). These attributes position iFlexSense as a promising tool for aerodynamic measurements in cryogenic engineering.

2. Materials and methods

2.1. Fabrication and encapsulation of single-layer films

Specifically, a 25 μm-thick Kapton PI film (Kapton HN, DuPont, USA) was selected, owing to its demonstrated ability to retain elasticity at temperatures as low as 4.2 K [56]. The PI film was first surface-activated using oxygen plasma (200 W, 3 min) in a reactive-ion etcher (Etchlab 200, SENTECH, Germany), and a Cr/Au (50/200 nm) electrode layer was subsequently deposited via magnetron sputtering (Pudi, China). Following that, to define the electrode geometry (power: 5%, frequency: 400 kHz, speed: 1000 mm·s^{-1}) and cut the film's outer contour (power: 50%, frequency: 400 kHz, speed: 1000 mm·s^{-1}, 10 passes), the resulting metallized PI film was patterned using a picosecond UV laser cutter (YLCF550UV-PS, Yuanlu, China). Electrode encapsulation was performed using a custom-built electrospray platform to deposit a PI precursor solution (ZKPI-3040, POME, China). A stainless-steel shadow mask protected areas not intended for deposition. Electrospray parameters included: voltage of 4000 V, needle-to-substrate distance of 3 cm, and substrate speed of 0.1 mm·s^{-1}. Upon mask removal, the film was cured in an oven (MD-40G, Hefei Zhenping, China) with a heating ramp of 5 °C·min^{-1}, including a pre-bake at 70 °C for 30 min and a final imidization at 250 °C for 240 min. This process yielded a single-layer film with a PI droplet encapsulation structure. The bottom electrode and cavity layers were fabricated via an analogous method.

2.2. Multilayer assembly of the iFlexSense

To assemble the multilayer skin, surfaces of the fabricated films were selectively masked using a stainless-steel shadow mask to protect microfluidic channels and electrode regions. A fully cyclized PI solution (ZKPI-810, POME, China) was then electrosprayed twice as an adhesive (voltage: 5000 V, distance: 3 cm, speed: 0.1 mm·s^{-1}). The films were soft-baked at 95 °C for 1 min. Subsequently, the two layers were aligned and pre-bonded on a 95 °C hotplate under a 1 kg weight to promote initial adhesion. Following that, a 100 μm-thick indium sheet (In100, Xiyin, China), pre-cut with the laser and treated with flux (ET-811L, Xiyin), was placed at locations requiring vertical electrical interconnects. The entire stack was transferred to a vacuum hot-press (Qixing R32022020, Qi'en, China). The assembly was preheated to 100 °C for 5 min at 0.05 MPa, after which the temperature was ramped at 5 °C·min^{-1} to 200 °C and held for 2 h at 0.3 MPa. This process ensured complete curing of the PI adhesive. Electrical interconnection was realized using a indium sheet vacuum hot-pressed/soldered between the flexible electrode pad and the rigid lead, providing a ductile and cryogenically robust soft–rigid transition (Fig. S1 in Appendix A). To enhance measurement repeatability by minimizing polymer creep, the final skin was annealed at 200 °C for 24 h between two glass slides and then allowed to cool slowly with the furnace.

2.3. PI electrospray coverage analysis

The surface morphology of the electrosprayed PI was imaged utilizing a laser scanning confocal microscope (VK-X200K, Keyence, Japan) and scanning electron microscopy (SEM) system (SU3900, Hitachi, Japan). Using the Trainable Weka Segmentation plugin in ImageJ (National Institutes of Health, USA), the images were segmented into droplet and substrate regions, and the resulting binary image was analyzed in MATLAB (MathWorks, USA) using bwlabel and regionprops functions to quantify the area and equivalent diameter of individual PI features. The total coverage percentage was calculated and visualized by overlaying a blue mask onto the original micrograph (Fig. S2 in Appendix A).

2.4. Electrical and pneumatic interfacing

Electrical connections (Fig. S3(a) in Appendix A) were established by soldering the core of a coaxial cable to the sensor electrode using indium. The cable's shield was connected to the skin's ground layer. The connection joint was then reinforced with an ultra-low-temperature epoxy (YF-9189, Yuefu, China) and electrically isolated from the model using Kapton PI tape. For pneumatic interfacing (Fig. S3(b) in Appendix A), the skin was adhered to the model surface with the same epoxy, leaving the microchannel outlet area exposed. This outlet was aligned with a counterbored hole in the model, which was connected to a stainless-steel tube. A polytetrafluoroethylene (PTFE) tube was fitted onto the steel tube via an interference fit to route the reference pressure line outside the wind tunnel.

2.5. Sensor characterization

The reference pressure P_{ref} inside the sensor's microfluidic cavity was regulated using a pressure controller (PACE 5000, Druck, UK), and an inductance–capacitance–resistance (LCR) meter (TH2840NX, Tonghui, China) was employed to record multi-channel capacitance at a frequency of 1 kHz. Meanwhile, a programmable cryogenic test chamber (LRHS-101F-YD, Linpin, China) provided the controlled low-temperature environment. All cryogenic tests were performed in a dry nitrogen environment to suppress frosting. The sensing cavity was pressurized using dry N_2 supplied by the pressure controller. Moreover, a commercial cryogenic pressure sensor (CTL-375 M-0.7 MpaA, Kulite, USA) was used as a reference, excited with 10 V from a direct current (DC) power supply (E36312A, Keysight, USA), with its output acquired by a data acquisition card (PXIe-4309, NI, USA). The hermetic sealing performance of the sensor at different temperatures was evaluated by pressurizing the cavity to a fixed reference pressure P_{ref}, switching the controller to measurement mode, and recording the pressure drop over a 30 s interval to determine the average leak rate.

2.6. Calculation methods

2.6.1. Conformal wrapping criterion

A nacelle's outer surface represents a non-developable surface with a positive Gaussian curvature $K = \kappa_1\kappa_2 > 0$, where κ_1, $\kappa_2$are the two principal curvatures. According to Gauss's Theorema Egregium, it cannot be isometrically mapped onto a plane. Conformal wrapping of such a surface requires the characteristic width of a skin segment, l_{piece}, to be less than a critical width [57], $l_{\mathrm{piece\_critical}}$:

$$l_{\mathrm{piece\_critical}} = \min\left(l_{\mathrm{piece\_critical1}}, l_{\mathrm{piece\_critical2}}\right)$$

where $l_{\mathrm{piece\_critical1}}$ is limited by interfacial adhesion, and $l_{\mathrm{piece\_critical2}}$ is constrained by material failure. Based on prior work [58,59], these critical widths are given by:

$$l_{\mathrm{piece\_critical1}} = \sqrt[4]{\frac{128\gamma_{\mathrm{adhesion}}}{\bar{E}_{\mathrm{piece}} t_{\mathrm{piece}} K^2}}, \text{ if } \gamma_{\mathrm{adhesion}} \le \frac{\bar{E}_{\mathrm{piece}} t_{\mathrm{piece}} \varepsilon_{\mathrm{critical}}^2}{2}$$

$$l_{\mathrm{piece\_critical2}} = \sqrt{\frac{8\varepsilon_{\mathrm{critical}}}{|K|}}, \text{ if } \gamma_{\mathrm{adhesion}} > \frac{\bar{E}_{\mathrm{piece}} t_{\mathrm{piece}} \varepsilon_{\mathrm{critical}}^2}{2}$$

where $\gamma_{\mathrm{adhesion}}$ is the adhesion energy, t_{piece} is the film thickness, $\varepsilon_{\mathrm{critical}}$ is the critical failure strain, E_{piece} is Young's modulus, ν_{piece} is Poisson's ratio, and $\bar{E}_{\mathrm{piece}} = E_{\mathrm{piece}}/\left(1-\nu_{\mathrm{piece}}^2\right)$ is the plane-strain modulus.

2.6.2. Nonlinear calibration using neural network

A data set of capacitance versus pressure was generated. To prevent overfitting from the small sample size during neural network training, the data was augmented by adding random noise with a variance of 0.02 pF to the capacitance values. The number of augmented data points N_i for each pressure P_i was non-uniformly distributed according to the formula:

$$N_i = N_{\text{noise}}\left(\frac{\sigma(P_{\max} - P_i)}{P_{\max}} + 1\right)$$

where $P_{\max}$ is the maximum calibration pressure, σ is a non-uniformity factor (typically 3–5), and N_{noise} is a base number of noise points. This augmented data set was employed to train a two-layer BP neural network with Bayesian regularization. A 70% random subset of the data was adopted for training, which yielded a high-fidelity nonlinear calibration curve for the sensor.

2.6.3. Repeatability calculation

Based on n repeated loading cycles and a 2σ confidence interval (~95%), the repeatability was quantified using the repeatability standard deviation σ_{R} according to the formula:

$$\sigma_{\text{R}} = \pm \frac{2\sigma_{n-1}}{Y_{\text{FS}}} \times 100\%$$

where Y_{FS} is the full-scale output, and σ_{n-1} is the sample standard deviation of the *n* sensor outputs y_i, calculated using Bessel's correction:

$$\sigma_{n-1} = \sqrt{\frac{1}{n-1}\sum_{i=1}^{n}(y_i - \bar{y})^2}$$

where $\bar{y}$ is the arithmetic mean of the n sensor outputs.

2.6.4. Pressure coefficient calculation

For compressible flows ($\text{Ma} \geq 0.3$), the freestream static pressure (P_∞) is related to the total pressure (P_0) by the isentropic flow relation:

$$P_\infty = P_0\left(1 + \frac{\gamma - 1}{2}\text{Ma}^2\right)^{-\frac{\gamma}{\gamma-1}}$$

where γ is the ratio of specific heats (≈ 1.4 for nitrogen gas in cryogenic wind tunnel conditions). The dynamic pressure, q_∞, is given by:

$$q_\infty = \frac{1}{2}\rho_\infty V_\infty^2 = \frac{1}{2}\gamma P_\infty \text{Ma}^2$$

where ρ_∞ and V_∞ are the freestream density and velocity. The dimensionless pressure coefficient C_p was then calculated from the measured surface pressure P:

$$C_p = \frac{P - P_\infty}{q_\infty}$$

3. Results and discussion

3.1. Design of iFlexSense

The iFlexSense was specifically engineered to endure and operate reliably under the extreme cryogenic and high-pressure environments characteristic of state-of-the-art wind tunnels. The design principles focused on two key aspects: the micro-structural architecture of the individual sensing element and the macro-structural topology of the skin for conformal integration onto complex aerodynamic surfaces of aerodynamic model.

At the core of the sensor lies a capacitive transducer, whose performance is highly dependent on its encapsulation structure. Fig. 2(a) and Fig. S4 in Appendix A present a schematic comparison between a conventional, dense encapsulation layer and the novel droplet-encapsulation architecture proposed herein. The working principle of the sensor can be elucidated by considering its response across three distinct pressure regimes.

(1) Low-pressure regime: At initial, low pressures, the compliant upper electrode deflects toward the substrate but does not make physical contact with the encapsulation layer. The total capacitance, C, is effectively a series combination of the capacitance of the air gap, C_{air}, and that of the encapsulation layer, C_{PI}. For the droplet-encapsulated structure, C_{PI} represents the integrated equivalent capacitance of the PI micro-droplets and the air-filled interstices between them. The governing relationship is $C = (C_{\mathrm{air}} \cdot C_{\mathrm{PI}})/(C_{\mathrm{air}} + C_{\mathrm{PI}})$. With increasing applied pressure, the gap distance decreases, leading to a monotonic increase in C_{air} and thus the measured total capacitance C. In this pre-touchdown regime, the pressure-capacitance response of both the droplet-based and dense encapsulation methods exhibits fundamentally analogous behavior.

(2) Intermediate-pressure regime: With further increases in pressure, the central portion of the upper electrode establishes contact with the encapsulation layer. At this juncture, the capacitive behavior diverges considerably. The total capacitance becomes a parallel combination of the capacitance from the now-contacted central area, $C_{\mathrm{PI\_central}}$, and the remaining series-capacitance contribution from the non-contacted annular edge region, $C_{\mathrm{air\_edge}}$ and $C_{\mathrm{PI\_edge}}$. For a conventional dense encapsulation, the contacted central area becomes mechanically saturated; it can no longer deform significantly, indicating relatively constant $C_{\mathrm{PI\_central}}$. Further sensitivity is derived exclusively from the continued deflection of the peripheral, non-contacted region. In stark contrast, the porous, non-dense nature of the droplet encapsulation allows the contacted portion of the upper electrode to continue deforming into the interstitial voids between droplets. Accordingly, $C_{\mathrm{PI\_central}}$ continues to increase with applied pressure, yielding a markedly enhanced sensitivity in this intermediate, post-touchdown pressure range.

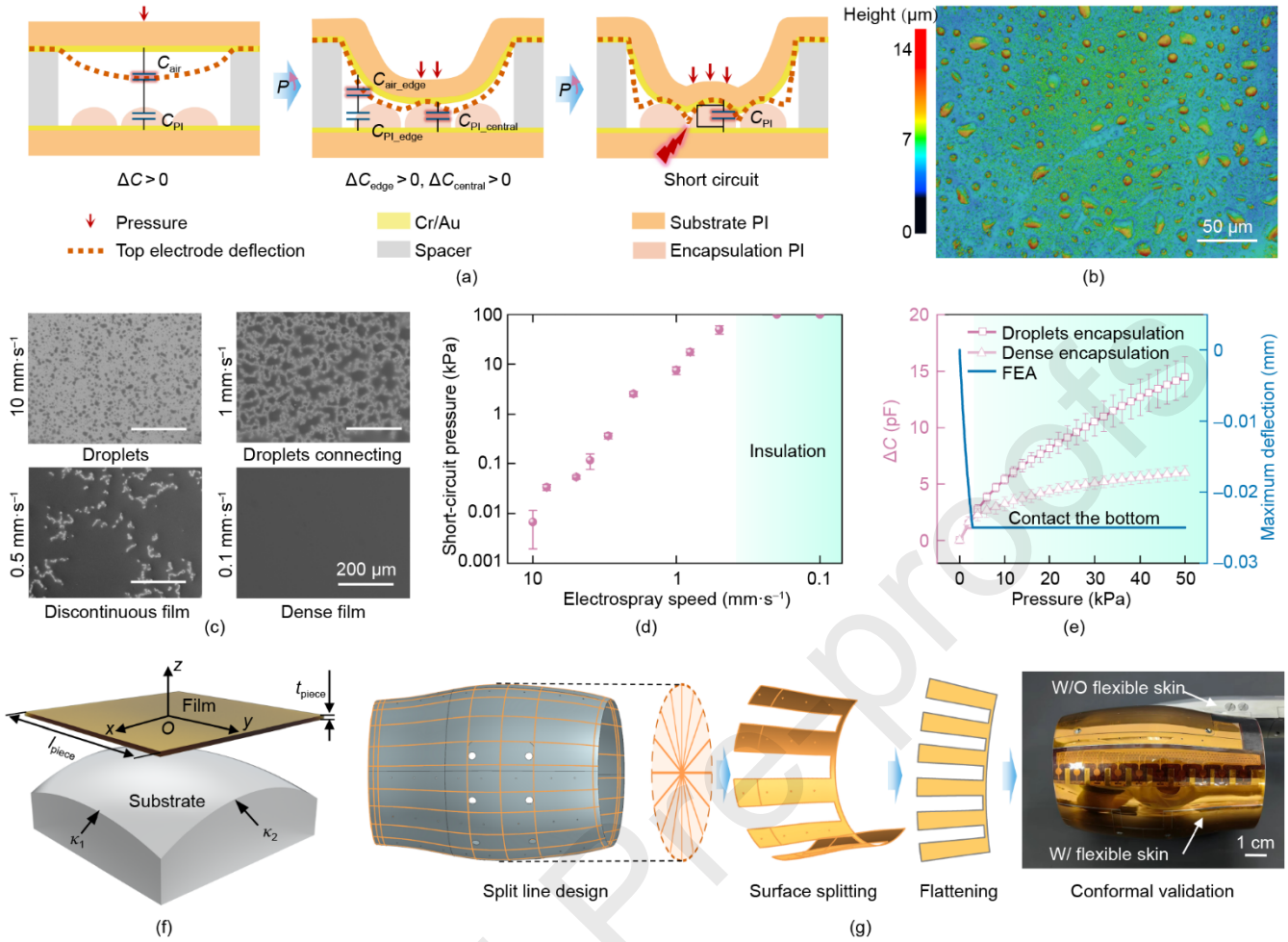

Fig. 2. Structural design of iFlexSense. (a) Schematic of sensitivity enhancement under high-pressure working range achieved by PI droplet encapsulation via electrospray. $\triangle C$: total capacitance change; $\triangle C_{edge}$: capacitance change from the edge region; $\triangle C_{central}$: capacitance change from the central region. (b) Contour map of the droplet-encapsulated surface. (c) SEM micrographs of surfaces prepared at different substrate moving speeds during electrospray. (d) Relationship between short-circuit threshold pressure and electrospray speed. (e) Comparison of capacitance–pressure responses for droplet and dense encapsulations, together with finite-element-analysis (FEA) simulations. (f) Schematic of the theoretical model for iFlexSense conformally attached to a wind tunnel model. (g) Design flowchart and conformal attachment validation of iFlexSense based on curvilinear conformal development. W/O: without; W/: with.

(3) High-pressure and failure regime: At sufficiently high pressures, the response of the densely encapsulated sensor becomes fully saturated, exhibiting a plateau in its capacitance output. While offering a wider dynamic range, the droplet-encapsulated sensor also has a failure threshold. Sufficiently high applied pressure deflects the upper electrode through the porous layer, establishing direct electrical contact with the bottom electrode and inducing a short circuit that eliminates sensing functionality. In essence, the droplet architecture strategically sacrifices certain ultimate over-pressure capacities to significantly boost sensitivity in the high-pressure operational range. This design trade-off is particularly advantageous for cryogenic wind tunnels, which frequently employ a synergistic combination of cooling and pressurization to achieve ultra-high Reynolds numbers.

The fabrication of this unique encapsulation morphology was achieved through the electrospraying of a PI precursor solution, a process to be detailed in the subsequent section. The resulting surface, as shown in the micrograph in Fig. 2(b) and Fig. S5 in Appendix A, was decorated with a field of PI micro-droplets, with diameters ranging from sub-micrometer to approximately 20 μm and heights on the order of micrometers. Precise modulation of the substrate traverse speed during electrospray deposition enabled accurate control over the surface morphology, representing a critical step in the fabrication process. As illustrated in Fig. 2(c) and Fig. S6 in Appendix A, a systematic evolution of the surface structure was observed. At high speeds, the deposition was sparse, resulting in discrete, isolated droplets. With reducing speed, the droplet density increased, leading to coalescence and the formation of interconnected “islands.” Further reduction in speed resulted in a continuous, porous network of PI. At very low speeds, the droplets fully merge and accumulate, forming a conventional dense

film. This exquisite control over the encapsulation morphology was directly linked to the sensor's short-circuit failure pressure, a key parameter for tailoring the sensor to a specific application's pressure range.

To maximize the performance enhancement offered by the droplet encapsulation, the short-circuit threshold pressure must be strategically set to be slightly greater than the sensor's intended measurement range. Therefore, the relationship between the electrospray speed and the resulting failure pressure was hereby systematically investigated, as plotted in Fig. 2(d). The data revealed a nearly log-linear relationship: a higher desired failure threshold necessitated a lower deposition speed, corresponding to a denser, more robust encapsulation layer. However, below a speed of 0.2 mm·s^{-1}, the layer became effectively dense and non-porous, remaining electrically insulating up to the 100 kPa limit of the test apparatus. According to the operational requirements of the target wind tunnels, which demand a positive pressure range of approximately 30–50 kPa, and considering the fixed sensor geometry (25 μm top PI film, 25 μm PI spacer), an optimal electrospray traverse speed of 0.5 mm·s^{-1} was determined. Compared to 0.1 and 0.2 mm·s^{-1}, the sample produced at 0.5 mm·s^{-1} exhibited enhanced sensitivity (Fig. S7 in Appendix A), as reduced surface PI coverage left more void space for deformation, increasing compliance and the effective gap change under pressure. However, excessively high traverse speed (> 0.5 mm·s^{-1}) yielded overly sparse droplets, leading to stress concentration and electrical short-circuit at high pressure. To experimentally validate the design superiority, a head-to-head comparison was performed between a sensor with the optimized droplet encapsulation and one fabricated with a conventional, spin-coated dense PI layer of comparable thickness (~1 μm). The results presented in Fig. 2(e) aligned perfectly with the theoretical model. In the low-pressure (< 4 kPa), pre-touchdown regime, the sensitivities of both sensors were nearly identical (0.636 vs 0.546 pF/kPa). However, once the applied pressure surpassed the touchdown threshold predicted by finite element analysis (FEA), the pressure response of the droplet-encapsulated sensor became significantly steeper, demonstrating its enhanced sensitivity (> 500%) in the higher-pressure domain (0.165 vs 0.0316 pF/kPa).

Beyond the micro-scale design of the sensing element, the macro-scale topology of the iFlexSense was engineered for seamless, conformal integration onto the non-developable, doubly-curved surface of the aircraft nacelle model. The allowable width of any given segment of the skin, l_{piece}, was constrained by the local surface curvature and the skin's material properties, as dictated by the conformal wrapping criterion detailed in Section 2. Given the skin's average thickness t_{piece} of approximately 98.4 μm (Fig. S8 in Appendix A), the maximum permissible width l_{piece} could be calculated. Based on such a constraint, a 2D planar split line was designed. This two-dimensions (2D) pattern was then computationally mapped onto the three-dimensions (3D) surface of the model using a curve projection algorithm to define the partitioned surface layout, as schematically shown in Fig. 2(f). The resulting planar skin contours were laser-cut, and the final design was validated and refined through a process of physical fitting and local optimization, ensuring a perfectly conformal, warp-free attachment to the model surface (Fig. 2(g)). Fig. S9 in Appendix A presents final fabricated iFlexSense topology. The full surface coverage design was considered critical, as it avoided the sharp edges and surface discontinuities associated with partially attached sensor patches, thereby minimizing any unintended disturbances to the boundary layer flow under investigation. Furthermore, the thickness used in this work (98.4 μm) yielded an root-mean-square error (RMSE) of C_p approximately 0.01, supporting aerodynamic non-intrusiveness for pressure mapping (Fig. S10 in Appendix A).

3.2. Fabrication process based on PI electrospraying

The successful realization of the all-PI iFlexSense benefits greatly from the versatile application of the PI electrospray technique. This technique is central to two critical fabrication steps: the formation of the functional droplet encapsulation layer, as discussed previously, and the creation of a robust, cryogenically-compatible adhesive bond for multilayer assembly. The overall fabrication workflow is depicted in Fig. 3(a) and described in Section 2. Herein, the process could be scaled up to meter-scale dimensions, with a manufacturing cost far below that of commercial rigid cryogenic pressure sensors.

Fig. 3(b) presents the principle of the electrospray apparatus. A high voltage was applied to a needle containing the PI solution. The strong electric field induced charge accumulation at the liquid's surface, deforming it into a conical shape known as a Taylor cone. When the electrostatic forces overcame the surface tension of the liquid, a fine jet was ejected from the cone's apex. This jet rapidly destabilized due to Coulombic repulsion among the induced charges, breaking up into a plume of charged micro- and nano-droplets [60] that were then guided by the electric field onto the grounded substrate, which was mounted on a programmable dual-axis motion stage. The structural PI layers in the device were fully imidized and chemically robust to PI droplets (Fig. S11 in Appendix A). Achieving a stable and continuous spray required operating within a specific process window of applied voltage and needle-to-substrate distance. The investigation of this process window is summarized in Fig. 3(c) and Fig. S12 in Appendix A. A larger distance generally increases the deposition area but requires a higher voltage

to maintain the field strength. To further quantify the process, the substrate speed was fixed at 1 mm·s^{-1} and systematically mapped the relationship between voltage, distance, and the resulting PI surface coverage, analyzed via computer vision techniques (Fig. 3(d) and Fig. S2 in Appendix A). As expected, the surface coverage increased with increasing voltage (stronger electrostatic pull) and decreasing distance (more focused deposition cone). Results revealed that reducing the needle-to-substrate distance was more effective for high coverage than increasing the voltage.

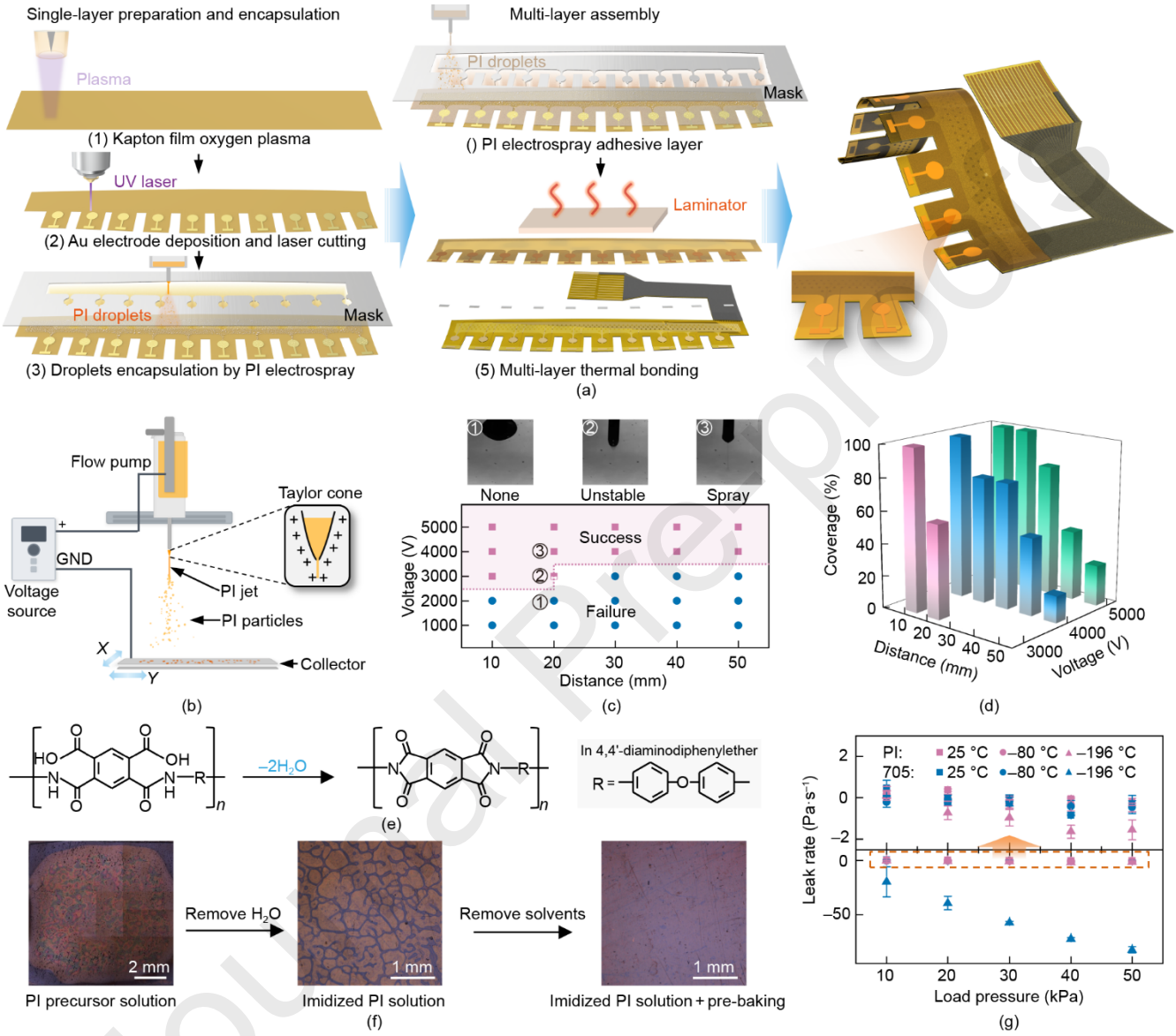

Fig. 3. Fabrication process based on PI electrospray. (a) Schematic illustration of the iFlexSense fabrication process flow. (b) Schematic diagram of the PI electrospray system. (c) Stable electrospray process window for PI, showing its dependence on applied voltage and nozzle-to-substrate distance. (d) Surface coverage of the PI electrospray as a function of applied voltage and nozzle-to-substrate distance. (e) Chemical structure of PI imidization. (f) Optical microscopy images of the interlayer sealing and adhesion using PI precursor, imidized PI solution, and pre-baked imidized PI solution. (g) Comparison of leak rates between PI-based adhesion and 705 silicone rubber adhesion under applied pressures of 10–50 kPa, from ambient to low-temperature conditions. Error bars represent the standard deviation of three independent measurements.

A second key application of PI electrospraying in this process was the deposition of the interlayer adhesive. The choice of an all-PI construction, including the adhesive, was deliberate. PI's unique combination of mechanical flexibility and chemical stability at deep cryogenic temperatures made it an ideal material for bonding and hermetically sealing the cavity structure of the capacitive sensor. However, conventional PI adhesives were supplied as polyamic acid precursors, which required a high-temperature curing step (imidization) to convert into the final, robust . This chemical reaction, a condensation

polymerization, released a significant amount of small water molecules as a byproduct (Fig. 3(e)). When this process occurred within a confined interface between two layers, the outgassing of water vapor at high temperatures created bubbles and voids, which compromised the bond's structural integrity and, critically, its hermeticity. This defect formation was clearly visible in Fig. 3(f). To overcome this fundamental challenge, a fully pre-imidized (or cyclized) PI solution was employed, which was already in its final chemical form and did not release water upon heating. While this solved the outgassing problem, the non-polar solvents used for such solutions could phase-separate during heating, creating a network-like structure that was also detrimental to sealing. The ultimate solution was a refined multi-step process: the fully cyclized PI solution was electrosprayed, followed by a gentle pre-baking step to remove the bulk of the solvent, and the final bonding stage was then conducted in a vacuum hot-press. The vacuum environment facilitated the removal of any residual solvent, resulting in a dense, void-free, and hermetically-sealed bonding interface.

To rigorously validate the cryogenic performance of this PI – PI bonding strategy, a comparative sealing performance test was further conducted against a commonly used cryogenic adhesive, 705 silicone rubber. The experimental procedure is detailed in the Section 2. As shown in Fig. 3(g), at both room temperature (25 °C) and a moderately low temperature of −80 °C, both the PI-bonded and silicone-bonded test devices exhibited excellent sealing performance, with leak rates consistently below 1 $Pa{\cdot}s^{-1}$ across various load pressures. This baseline leak rate approached the intrinsic leak rate of the measurement system. The critical test, however, came at the deep cryogenic temperature of −196 °C (liquid nitrogen). At this temperature, the leak rate of the silicone-sealed device dramatically increased by two orders of magnitude, indicating a catastrophic failure of the hermetic seal. This was likely attributed to a combination of embrittlement and a mismatch in the CTE between the silicone and the PI substrate, leading to interfacial delamination [61]. In striking contrast, the all-PI electrospray-bonded device maintained its excellent sealing performance, with a leak rate comparable to its room-temperature value. This result unequivocally demonstrated the superiority and feasibility of this all-PI bonding approach for applications in deep cryogenic environments.

3.3. Characterization of pressure sensing performance

A comprehensive characterization campaign was undertaken to validate the sensor's performance, first at ambient temperature and then across the full cryogenic range relevant to wind tunnel operations. The iFlexSense was distinguished by its ability to detect both positive and negative gauge pressures, enabling accurate characterization of complex pressure fields over aerodynamic surfaces with suction and compression zones. This was enabled by a microfluidic channel integrated into the skin [62], which allowed the internal reference pressure of the sensor's cavity, P_{ref}, to be precisely controlled by an external pressure source. This capability not only provided bipolar measurement but also allowed for on-demand extension of the sensing range and, most importantly, for rapid *in situ* calibration of the sensor immediately prior to a test run. To facilitate this, a dedicated deep-cryogenic, positive-and-negative pressure *in situ* calibration system was hereby designed and constructed, as detailed schematically in Fig. 4(a) and Fig. S13 in Appendix A. The system comprised a data acquisition and control unit, which managed the pressure controller and acquired sensor data, and a cryogenic test system. The latter used controlled liquid nitrogen injection and proportional–integral–derivative (PID) feedback from thermocouple probes to create a stable and uniform low-temperature environment for the sensor under test. The iFlexSense was mounted on a test fixture alongside a commercial, high-performance deep-cryogenic pressure sensor (Kulite CTL-375, Kulite Semiconductor Products, USA; a silicon piezoresistive type) to allow for simultaneous, cross-referenced pressure loading and data acquisition (Fig. 4(b)).

First, the sensor's baseline performance was thoroughly characterized at room temperature. Fig. 4(c) presents the calibration results for a positive pressure range up to 50 kPa and a negative pressure range down to −30 kPa. The sensitivity under negative gauge pressure was lower because the diaphragm deflected away from the counter-electrode, increasing the dielectric gap and yielding a more gradual (bounded) capacitance decrease. In contrast, positive pressure drove the diaphragm toward touchdown, producing a steeper response. Considering the inherent stochastic component of electrospray deposition, unit-to-unit consistency was hereby evaluated by fabricating multiple sensors under identical electrospray parameters and comparing their pressure–capacitance responses (Fig. S14 in Appendix A). The response trend and touchdown transition exhibited good repeatability, while the absolute capacitance level and the exact touchdown pressure varied slightly among units due to local differences in droplet density and effective dielectric thickness. Accordingly, each sensing node was calibrated individually, and the Backpropagation Neural Network (BPNN)-based calibration framework was trained per node to ensure high-fidelity pressure reconstruction. To address this, the Bayesian regularized BPNN was trained per node to ensure high-fidelity pressure reconstruction, as detailed in Section 2. Given the relatively small number of calibration points typically acquired, there existed a high risk of overfitting the model. This was mitigated by employing a weighted noise injection technique for data augmentation. This method artificially expanded the training data set while preserving the

underlying pressure-capacitance relationship, significantly improving the robustness and generalization capability of the resulting calibration model (Fig. S15 in Appendix A). This approach proved highly effective, yielding a high-fidelity fit with a maximum error of only ~10 Pa across the entire calibration range for different sensor units. To verify structural recovery after compression, confocal profilometry was performed on the same sensing region at multiple pressures and after unloading. The surface height maps (Fig. S16 in Appendix A) indicated that the deformation was predominantly elastic within 0–50 kPa and that the top PI substrate recovered close to its initial profile after unloading.

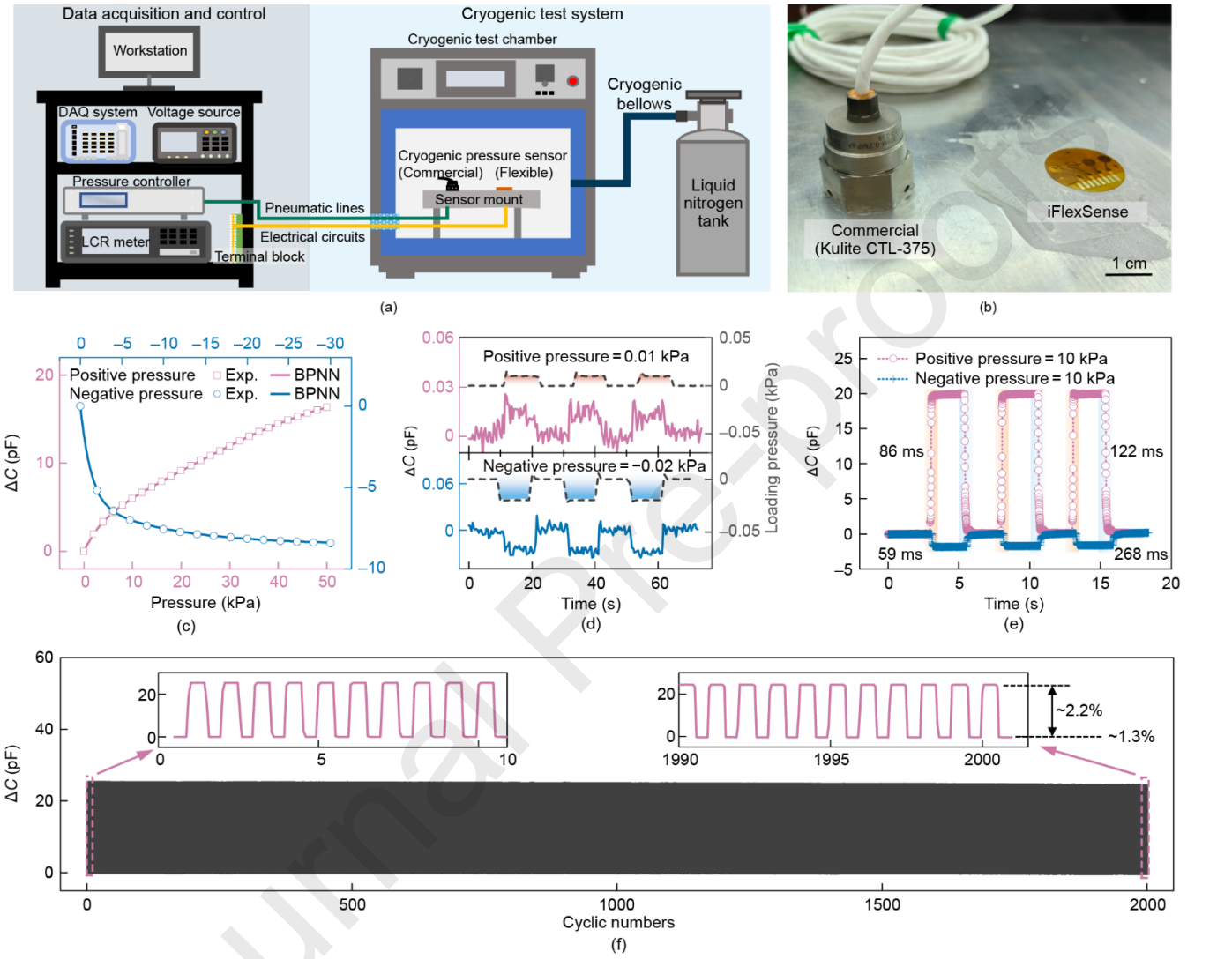

Fig. 4. Pressure sensing performance characterization. (a) Schematic of the cryogenic *in-situ* positive and negative pressure calibration system. (b) Photograph of a commercial Kulite cryogenic pressure sensor and the iFlexSense installed within the cryogenic test system. (c) Capacitance change as a function of positive and negative pressure. The BPNN denotes a backpropagation neural network-based nonlinear fitting. (d) Limit of detection (LOD) for both positive and negative pressures. (e) Response and recovery times under 10 kPa positive and negative pressure. (f) Stability test conducted over 2000 cycles of 10 kPa pressure loading.

Key performance metrics were subsequently quantified. The sensor's limit of detection (LOD) was tested by applying small, repeated pressure steps. As shown in Fig. 4(d), the sensor could clearly and repeatedly resolve positive pressure steps of 0.01 kPa (equivalent to 0.02% of full scale, FS) and negative pressure steps of 0.02 kPa (0.067% FS). The sensor's temporal response was characterized by actuating a fast-switching electronic valve in the pressure controller to generate a step-like change in pressure within the sensor cavity. Results are shown in Fig. 4(e) and Fig. S17 in Appendix A. Under a 10 kPa pressure step, the 10%–90% rise times during loading were 86 and 59 ms for positive and negative pressures, respectively. The corresponding fall times upon unloading were prolonged to 122 and 268 ms. Notably, these measured times were system-level response ones and included latencies from the valve's mechanical switching, the gas transit time through the tubing, and the time required for the pressure to equilibrate within the cavity. The intrinsic response time of the capacitive membrane

itself was significantly faster. Nevertheless, for quasi-steady static pressure measurements in wind tunnels, where data was typically averaged over seconds, a response time of tens to hundreds of milliseconds was more than sufficient. Considering the high-temperature annealing step included in the fabrication process (Section 2), the PI material exhibited low creep and high elastic recovery. The sensor's long-term stability was validated by subjecting it to a fatigue test, consisting of 2000 cycles of 10 kPa pressure loading and unloading (Fig. 4(f)). Following the full test, the sensor's baseline output had drifted by a mere 1.3%, and its response amplitude had changed by merely 2.2%. This level of stability was generally acceptable for a single wind tunnel test campaign. To ensure the highest accuracy across multiple test campaigns over extended periods, the *in situ* calibration capability allowed for a fresh, accurate calibration to be performed in minutes by simply sweeping the reference pressure P_{ref}.

While room-temperature performance provided a baseline, the characterization under cryogenic conditions was still considered the most critical validation. Herein, a comprehensive thermal characterization was further performed by comparing the iFlexSense's response with the commercial Kulite sensor while sweeping the temperature from 50 °C down to −190 °C (Fig. 5(a)). At each temperature setpoint, the system was allowed to thermally equilibrate for 15 min before a stepped pressure profile (0 to 20 kPa in 2 kPa increments) was applied. The apparent capacitance fluctuation observed during the cooling from 50 to −10 °C was not an intrinsic instability, but mainly originated from the nitrogen cold-gas jet onto the iFlexSense mounted facing upward. The iFlexSense successfully tracked the pressure steps at all temperatures. Remarkably, the signal-to-noise ratio of the flexible sensor remained comparable to that of the high-end commercial sensor even at the extreme low temperature of −190 °C (Fig. 5(b)). Consistent with typical polymer-based sensors, the iFlexSense displayed significant temperature dependence, contrasting with the custom-fabricated, temperature-compensated silicon piezoresistive sensor (Fig. S18 in Appendix A). With decreasing temperature, the polymer chains in the PI film exhibited reduced thermal energy and mobility, leading to an increase in the material's macroscopic stiffness. This stiffening of the sensor's diaphragm exerted a direct impact on its performance: the sensor's sensitivity decreased, yet its linearity improved, considering the smaller deflections for a given pressure (Fig. 5(c) and Fig. S19 in Appendix A). In the deep-cryogenic regime (approximately below −80 °C), the baseline drift per degree was smaller compared to the situation during the room-temperature-to-subzero cooling segment (Fig. S20 in Appendix A). This implied that for accurate wind-tunnel measurements, the iFlexSense required *in situ* recalibration after the tunnel stabilized at its target cryogenic operating temperature. This was a standard procedure in high-precision testing and could be performed quickly at low-speed ($\mathrm{Ma} < 0.15$) or zero-flow conditions. A typical calibration sequence (e.g., 25 pressure steps spanning the operating range) could be completed in ~5 min for all channel and was employed to train the unit-specific BPNN calibration model. Upon calibration under low-speed conditions, the calibration error induced by temperature variations remained within an acceptable range for temperature changes within 10 °C (Fig. S21 in Appendix A). To confirm the absence of any thermal hysteresis, the sensor's calibration curve was monitored after returning to room temperature from −190 °C. As shown in Fig. 5(d), the curve nearly overlaid the initial room-temperature curve, although a slight decrease in sensitivity was observed during the warming phase compared to the cooling phase. This minor discrepancy was likely attributable to thermal gradients within the test chamber, requiring extended equilibration times.

To further address the dynamic performance under cryogenic conditions, the response and recovery times of iFlexSense at different temperatures were quantified (Fig. S22 in Appendix A). Notably, the response-time measurement in cryogenic tests was not identical to that used in Fig. 4(e) and thus the values were not directly comparable. Specifically, vent-to-ambient unloading was avoided at deep-cryogenic temperatures, as it might introduce moisture into the pneumatic line and cause condensation/icing inside the cavity and tubing. Therefore, both pressure loading and unloading were realized by adjusting the pressure controller output in the control mode, and the extracted response time reflected the overall system response (pressure controller + pneumatic line/pneumatic volume + sensor), rather than the intrinsic membrane response alone. Even under this system-limited measurement, the response time during unloading showed a decreasing trend as temperature decreased. This indicated that cryogenic operation did not impair the sensor dynamics. Indeed, the increased PI modulus at low temperatures increased the structural natural frequency, which was favorable for fast intrinsic response. Coupled with the improved linearity observed at cryogenic temperatures, these results confirmed the suitability of iFlexSense for transient pressure measurements in cryogenic wind-tunnel environments. To further benchmark the ultimate cryogenic limit, the sensor was also immersed in liquid nitrogen (−196 °C), and stepped pressure loading was performed; the device remained functional and showed clear step outputs (Fig. S23 in Appendix A).

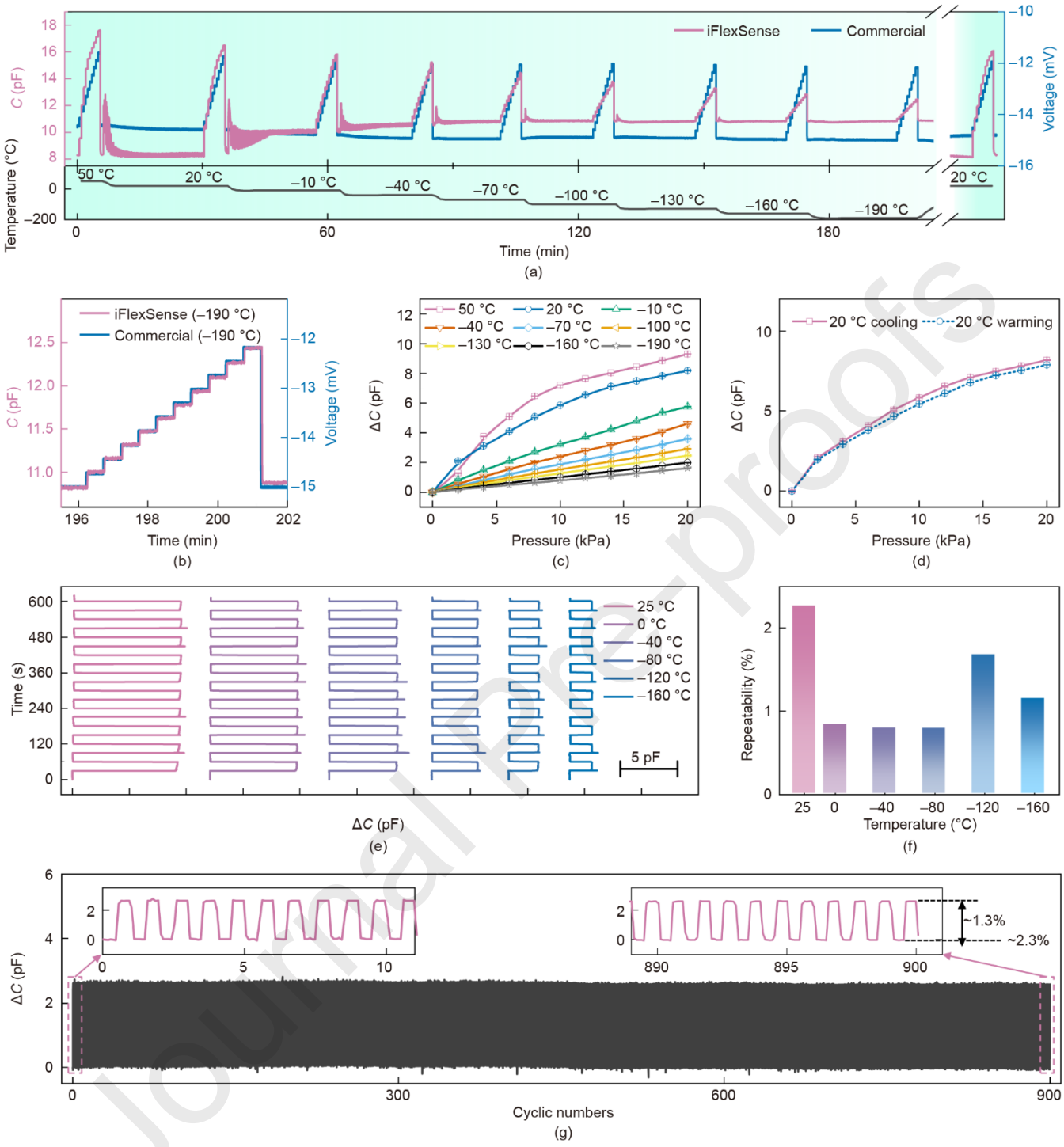

Fig. 5. Cryogenic performance characterization. (a) Response of the iFlexSense and a commercial cryogenic pressure sensor to 0–20 kPa pressure step loading, as the temperature varies from 50 to −190 °C. (b) Comparison of pressure response signals between the iFlexSense and the commercial cryogenic pressure sensor at an extreme temperature of −190 °C under 2 kPa pressure steps. (c) Calibration curves of capacitance change versus applied pressure for the iFlexSense across temperatures ranging from 50 to −190 °C. (d) Calibration curves at room temperature before and after cryogenic cycling to −190 °C, confirming the absence of thermal hysteresis. (e) Stability test conducted over 10 cycles of 10 kPa repeated loading at temperatures from 25 to −160 °C. (f) Standard deviation of repeatability across the temperature range of 25 to −160 °C. (g) Deep-cryogenic cyclic loading repeatability at −190 °C for 900 cycles.

Finally, the sensor's measurement repeatability under cryogenic conditions was quantified. At each target temperature, the sensor was subjected to 10 repeated loading cycles of 10 kPa (Fig. 5(e)). The repeatability standard deviation, σ_R, was calculated from the data. To exclude the transient effects of the pressure controller's overshoot, only the stable, middle 20 s

portion of each 30 s loading phase was employed for the calculation. The results, as plotted in Fig. 5(f), showed that the σ_R remained below 2.5% at all tested temperatures. To evaluate deep-cryogenic repeatability, 900 loading/unloading cycles were performed at −190 °C under 10 kPa. The sensitivity change after cycling was 1.3%, and the zero-offset drift was 2.3%, indicating robust cyclic stability at deep cryogenic temperature (Fig. 5(g)). These demonstrated the excellent stability and reliability of the iFlexSense for rendering repeatable, quantitative measurements in a deep cryogenic environment.

3.4. Cryogenic wind tunnel experiments

The high-Reynolds-number simulation capability of cryogenic wind tunnels represents an indispensable tool in the aerospace industry, particularly for advancing large transport aircrafts [63]. To demonstrate its real-world applicability, the fully characterized deep-cryogenic iFlexSense was deployed in two different cryogenic wind tunnel facilities. The first was the 0.3 m continuous-flow transonic cryogenic wind tunnel [64] (Fig. 6(a)), where the iFlexSense was conformally applied to a custom-designed aircraft nacelle model (Fig. 6(b)). The model was instrumented with seven conventional static pressure taps, whose locations (normalized by the chord length, x/c, where x is the chordwise distance from the leading edge and c is the chord length) are listed in Table S2 in Appendix A, to serve as a ground-truth reference (Fig. 6(c)). The iFlexSense was transferred from a flat substrate to the curved model surface, with visual alignment employed to minimize excessive positioning errors (Fig. S24 in Appendix A). The second facility was a 0.1 m cryogenic wind tunnel (Fig. S25 in Appendix A). Considering its smaller test section cross-area, a NACA 0012 semi-span wing model was selected to mitigate flow blockage effects, mounted directly to the tunnel wall. This model was similarly instrumented with four pressure taps for comparative measurements (Table S2 in Appendix A). For both installations, the skin's delicate electrical and pneumatic interfaces were protected from the cryogenic flow using the methods described in Section 2 (Fig. S3 in Appendix A) and routed through the model's support strut to the data acquisition systems outside the tunnel. One critical operational challenge in wind tunnels was the large and rapid variation in total pressure during startup and shutdown. To protect the skin's delicate membrane from potentially damaging rapid change in total pressure, a pressure-following system (Fig. S26 in Appendix A) was designed and implemented. This system utilized a set of three valves to intelligently manage the sensor's internal reference pressure, ,*P*-ref.. By selectively connecting the sensor cavity to either the pressure controller (for calibration/measurement), the plenum chamber pressure (,*P*-chamber.), or venting to atmosphere, the system could operate in multiple modes. During periods of changing tunnel conditions, the system entered a "pressure-following" mode by connecting ,*P*-ref. to ,*P*-chamber.. Given that ,*P*-chamber. closely tracked the freestream total pressure, this ensured small and positive pressure differential across the sensor membrane, effectively safeguarding it from destructive loads.

The results from a series of typical wind tunnel tests are presented in Figs. 6(d)–(f), where all measured pressure data was converted to the non-dimensional pressure coefficient, C_p, to facilitate aerodynamic analysis. The test campaigns covered an extensive operational envelope, with total temperatures (T_0) ranging from 300 K down to 110 K, total pressures (P_0) from 115 to 450 kPa, and freestream Mach numbers (Ma) from 0.6 to 1.3. Figs. 6(d) and (e) presents the data from the 0.3 m tunnel with the nacelle model, while results from the 0.1 m tunnel with the NACA 0012 wing are illustrated in Fig. 6(f). At subsonic conditions (Fig. 6(d)), the pressure distribution over the nacelle exhibited a characteristic negative C_p peak, corresponding to the acceleration of the flow over the curved surface, followed by a pressure recovery (deceleration) downstream. In the supersonic regime (Fig. 6(e)), the pressure coefficient in the measured region exhibited a monotonic decrease, a feature linked to the interaction of the shock wave system with the boundary layer, which would be discussed further below. The surface pressure distribution on the NACA 0012 wing (Fig. 6(f)) exhibited a robust suction peak near the leading edge, which was consistent with classic airfoil theory and previous experimental studies. Across this entire, diverse set of aerodynamic and thermodynamic conditions, the measurements from iFlexSense showed excellent quantitative agreement with the data from the co-located, high-precision pressure scanner. The RMSE in C_p between the two measurement techniques was consistently below 0.05. This excellent agreement firmly validated the accuracy of the sensing skin and demonstrated its potential as a dependable measurement tool for harsh cryogenic wind tunnel environments.

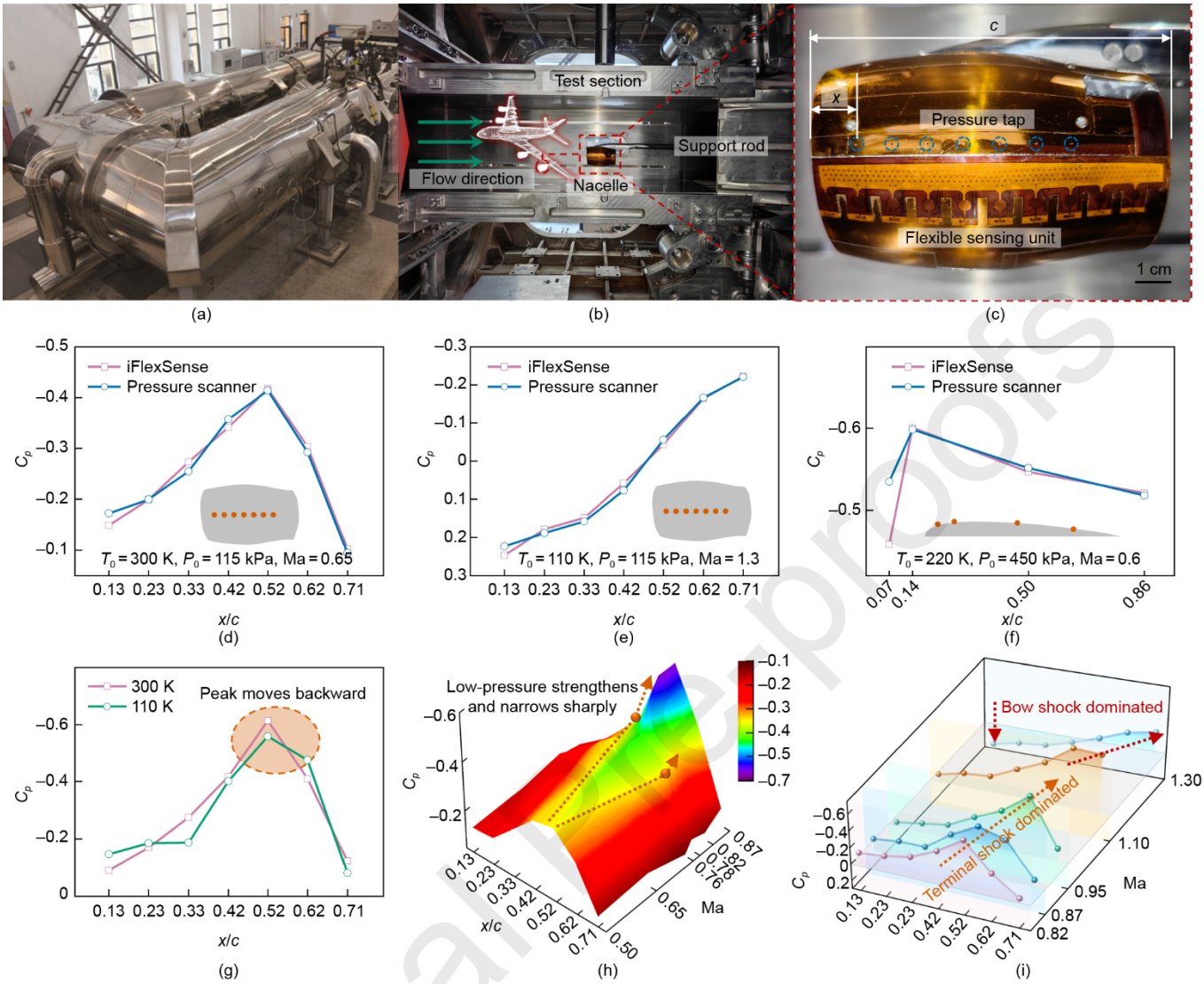

Fig. 6. Surface static pressure measurement in cryogenic wind tunnel. (a) Photograph of the 0.3 m continuous-flow transonic cryogenic wind tunnel [51]. (b) Setup of the test section in the 0.3 m cryogenic wind tunnel. (c) iFlexSense attached to the nacelle surface alongside configured pressure taps. (d – f) Pressure coefficient (C_p) distribution versus normalized chord coordinate (x/c) under typical wind tunnel conditions: (d) 0.3 m cryogenic wind tunnel, with total temperature (T_0) = 300 K, total pressure (P_0) = 115 kPa, and Mach number (Ma) = 0.65. (e) 0.3 m cryogenic wind tunnel, T_0 = 110 K, P_0 = 115 kPa, Ma = 1.3. (f) 0.1 m cryogenic wind tunnel, T_0 = 220 K, P_0 = 450 kPa, Ma = 0.6. (g) Reynolds number effect validation by comparing surface pressure distributions at P_0 = 115 kPa and Ma = 0.87 for T_0 = 300 K and 110 K in the 0.3 m cryogenic wind tunnel. (h) Effect of shock wave formation on surface C_p distribution during the subsonic phase (Ma = 0.5–0.87). (i) Evolution of shock waves and its impact on surface C_p distribution during the transonic phase (Ma = 0.82–1.3).

Beyond simple validation, the capacity to capture subtle, physically significant aerodynamic phenomena was demonstrated. One such phenomenon was the Re effect, investigated by comparing the surface pressure distribution on the nacelle at a fixed Mach number (Ma = 0.87) and total pressure (P_0 = 115 kPa), but at two different total temperatures: T_0 = 300 K (room temperature) and T_0 = 110 K (cryogenic). The decrease in temperature increased the fluid density and decreased its viscosity, leading to a significant increase in the test Re. The results, plotted in Fig. 6(g) and Fig. S27 in Appendix A, revealed a subtle yet distinct change: at the colder, high-Re condition, the low-pressure region was shifted slightly toward the trailing edge. However, the magnitude was subtle and close to the spatial resolution limit of the present sensing-node density. Therefore, the trend was interpreted qualitatively, and CFD was utilized as a consistency check rather than as a statistically definitive measurement (Fig. S28 in Appendix A). This aerodynamic phenomenon could be explained by boundary layer theory: the elevated Reynolds number led to a thinner, more energetic boundary layer that exhibited enhanced resistance to flow separation. This, in turn, affected the position where the shock wave formed and induced separation, causing the resulting low-pressure region to be located further downstream.

Finally, the high spatial and temporal resolution of the iFlexSense was leveraged to study the evolution of surface aerodynamic phenomena during the transition from subsonic to supersonic flight. In the 0.3 m tunnel at T_0 = 300 K and P_0 = 115 kPa, a Mach number sweep was performed from Ma = 0.5 up to 0.87 (Fig. 6(h)). A dramatic change in the pressure distribution occurred around Ma = 0.82. The broad, smooth low-pressure region transformed into a very sharp, narrow suction peak located at x/c = 0.52. This was the aerodynamic signature of the formation of a local supersonic flow region on the model's surface, terminated by a shock wave. This shock wave interacted with the boundary layer, inducing a small separation bubble, which resulted in the sharp pressure drop, or suction peak. Then, the behavior in the transonic-to-supersonic phase at a cryogenic temperature of T_0 = 110 K was investigated (Fig. 6(i)). As the Mach number approached unity, the suction peak increased in magnitude and gradually shifted toward the trailing edge, signifying the intensification and downstream migration of shock-induced flow separation. As the freestream Mach number crossed 1.0, the flow physics changed again. The suction peak vanished entirely, and the pressure distribution became characterized by a high-pressure region at the front, followed by a gradual decrease. This occurred because, in supersonic flight, a detached bow shock formed ahead of the nacelle's leading edge. This strong shock decelerated the flow passing through it to subsonic speeds, and the terminal shock system on the surface disappeared. By accurately capturing the complex, dynamic evolution of surface pressure distributions during shock wave formation and development, the iFlexSense offered a novel and powerful experimental approach for aerodynamic investigations. The successful cross-validation with pressure taps and the detailed capture of both the Re effect and shock dynamics firmly establish the skin's capability for precise, quantitative wind tunnel testing, signifying its importance for future studies of advanced aircraft in cryogenic facilities.

4. Conclusions

This work presented the development and validation of iFlexSense, a fully PI-based flexible pressure sensing skin, specifically designed for high-fidelity aerodynamic measurements in the extreme conditions of cryogenic wind tunnels. This approach overcame critical material and performance challenges associated with extreme cold by innovatively leveraging PI electrospraying for both a unique droplet-encapsulation sensing structure and for robust interlayer bonding. This all-PI construction ensured outstanding mechanical flexibility and resilience down to −196 °C, effectively preventing the embrittlement and delamination issues that plagued conventional flexible sensors. A key innovation, the droplet-encapsulation method, enhanced sensor sensitivity in the high-pressure working range—a vital feature for high-Reynolds-number testing—without compromising performance in low-pressure working range.

The practical applicability and accuracy of the skin were rigorously demonstrated through experiments in 0.1 m and 0.3 m cryogenic wind tunnels. Across a wide operational range of temperature, pressure, and Mach number, the skin's measurements showed excellent agreement with traditional pressure tap data (RMSE in C_p < 0.05). Furthermore, the iFlexSense successfully captured complex flow physics, including subtle Reynolds number effects and shock wave dynamics. Notably, the present validation focused on cryogenic transonic conditions with weak aerodynamic heating. In high-Mach/hypersonic flows characterized by substantial aerodynamic heating, severe thermal gradients, and extremely thin boundary layers, the present polymer-based sensing skin might not be directly applicable. While demonstrated here in wind tunnels, the all-PI design strategies—specifically the droplet-encapsulation and electrospray bonding—could still provide a generalized solution for flexible electronics in extreme environments. Collectively, this work establishes iFlexSense not only as a verified instrument for aerodynamics but also as a promising platform for structural health monitoring and environmental sensing across the broader field of cryogenic engineering.

Acknowledgments

This work was supported by the National Natural Science Foundation of China (52427809, 52375568, and 52525502), and the Science and Technology Innovation Team of Hubei Province. The authors acknowledge the Flexible Electronics Manufacturing Laboratory in Comprehensive Experiment Center at Huazhong University of Science and Technology for its support in advanced manufacturing equipment.

Compliance with ethics guidelines

Lang Yin, Fan Zhang, Jiayang Li, Huamin Yu, Peng Qiao, Shuchuan Li, Huinan Zhang, Yaning Zheng, Zhangyu Xu, Mengfei Yin, Xuejun Liu, Hanqing Liu, Yuxin Guo, Jingjing Ji, Guoshuai Li, Dawei Liu, and YongAn Huang declare that they have no conflict of interest or financial conflicts to disclose.

References

[1] Zohuri B. Physics of cryogenics: an ultralow temperature phenomenon. Amsterdam: Elsevier; 2017.

[2] Goodyer MJ. The cryogenic wind tunnel. Prog Aerosp Sci 1992;29(3):193–220.

[3] Wertz JR, Larson WJ. Space mission analysis and design. 3rd ed. Dordrecht: Springer; 1999.

[4] Kamerlingh Onnes H. Further experiments with liquid helium. C. On the change of electric resistance of pure metals at very low temperatures etc. IV. The resistance of pure mercury at helium temperatures. In: Gavroglu K, Goudaroulis Y, editors. Through measurement to knowledge. Dordrecht: Springer; 1991. p. 261–3.

[5] Vos JB, Rizzi A, Darracq D, Hirschel EH. Navier–Stokes solvers in European aircraft design. Prog Aerosp Sci 2002;38(8):601–97.

[6] Blackwell JA. Preliminary study of effects of Reynolds number and boundary-layer transition location on shock-induced separation. In: Proceedings of the Specialists" Meeting on Transonic Aerodyn; 1968 Sep 1; Paris, France. Washington, DC, NASA; 1969.

[7] Kong WJ, Dong H, Zhao YD, Wu JF. Skin friction measurement and drag reduction of porous media under cryogenic and high Reynolds number conditions. Acta Aerodyn Sinica 2024;42(8):84–92.

[8] Guo Q, Feng S, Wang J. Effects of 3-D deformation of elastic wings on aerodynamic performance of an aircraft model. Sci China Technol Sci 2023;66(5):1365–77.

[9] Green J, Quest J. A short history of the European Transonic Wind Tunnel ETW. Prog Aerosp Sci 2011;47(5):319–68.

[10] Kulkarni M, Edward S, Golecki T, Kaehr B, Golecki H. Soft robots built for extreme environments. Soft Sci 2025;5(1):12.

[11] Nguyen TK, Phan HP, Dinh T, Dowling KM, Foisal ARM, Senesky DG, et al. Highly sensitive 4H-SiC pressure sensor at cryogenic and elevated temperatures. Mater Des 2018;156:441–5.

[12] Zhang K, Li J, Chen X. Effect of static pressure measurement errors from wall taps on cryogenic supercritical helium flow measurement in Venturi flowmeters. Flow Meas Instrum 2025;106:103004.

[13] Yorita D, Klein C, Henne U, Ondrus V, Beifuss U, Hensch AK, et al. Successful application of cryogenic pressure sensitive paint technique at ETW. In: Proceedings of the 2018 AIAA Aerospace Sciences Meeting; 2018 Jan 8–12; Kissimmee, FL, USA. Reston: AIAA; 2018.

[14] Luo Y, Abidian MR, Ahn JH, Akinwande D, Andrews AM, Antonietti M, et al. Technology roadmap for flexible sensors. ACS Nano 2023;17(6):5211–95.

[15] Huang Y, Zhu C, Xiong W, Wang Y, Jiang Y, Qiu L, et al. Flexible smart sensing skin for “Fly-by-Feel” morphing aircraft. Sci China Technol Sci 2022;65(1):1–29.

[16] Lee JH, Cho K, Kim JK. Age of flexible electronics: emerging trends in soft multifunctional sensors. Adv Mater 2024;36(16):2310505.

[17] Hurdoganoglu D, Safaei B, Cheng J, Qin Z, Sahmani S. A comprehensive review on the novel principles, development and applications of triboelectric nanogenerators. Appl Mech Rev 2024;76(1):010802.

[18] Wang B, Zhang B, Wu X, Zhou Y, Xiao L, Jiang S, et al. Design criteria for conformal integration of flexible electronics on advanced aircraft surfaces. Int J Mech Sci 2024;277:109448.

[19] Xiao L, Cheng M, Chen F, Jiang S, Huang Y. Theoretical modeling of conformal criterion for flexible electronics attached onto complex surface. J Appl Mech 2022;89(3):031005.

[20] Wang S, Wang Y, Chen Z, Mei D. Kirigami design of flexible and conformal tactile sensor on sphere-shaped surface for contact force sensing. Adv Mater Technol 2023;8(3):2200993.

[21] Wang H, Wu H, Ye D, Zhao C, Wu Q, Wang S, et al. Micro-cylindrical/fibric electronic devices: materials, fabrication, health and environmental monitoring. Soft Sci 2024;4(4):41.

[22] He X, Cai J, Liu M, Ni X, Liu W, Guo H, et al. Multifunctional, wearable, and wireless sensing system via thermoelectric fabrics. Engineering 2024;35:158–67.

[23] Chen Y, Cao J, Qiu J, Yang D, Liu M, Zhang M, et al. Capacitive in-sensor tactile computing. Nat Commun 2025;16(1):5691.

[24] Xu Z, Zhang F, Xie E, Hou C, Yin L, Liu H, et al. A flexible, large-scale sensing array with low-power in-sensor intelligence. Research 2024;7:0497.

[25] Wang Y, Qiu L, Luo Y, Ding R. A stretchable and large-scale guided wave sensor network for aircraft smart skin of structural health monitoring. Struct Health Monit 2021;20(3):861–76.

[26] Yin L, Wang Y, Zhan J, Bai Y, Hou C, Wu J, et al. Chest-scale self-compensated epidermal electronics for standard 6-precordial-lead ECG. npj Flex Electron 2022;6(1):29.

[27] Xuan Y, Uchiyama T, Ura H, Hagiwara S, Kato H, Sarkar SK, et al. Flexible integrated air pressure sensors for monitoring positive and negative pressure distribution. ACS Appl Mater Interfaces 2024;16(40):54215–23.

[28] Wang J, Wei X, Shi J, Bai N, Wan X, Li B, et al. High-resolution flexible iontronic skins for both negative and positive pressure measurement in room temperature wind tunnel applications. Nat Commun 2024;15(1):7094.

[29] Sun B, Ma B, Wang P, Luo J, Deng J, Gao C. High sensitive flexible hot-film sensor for measurement of unsteady boundary layer flow. Smart Mater Struct 2020;29(3):035023.

[30] Pang P, Zhang T, Zhang X, Ma B, Zhao K, Deng J, et al. Constant temperature hot-film sensor for the measurement of near-wall turbulence and flow direction. IEEE Sens J 2024;24(5):5895–903.

[31] Sheng H, Cao LNY, Shang Y, Li C, Zhou Z, Jiang Y, et al. Conformal self-powered high signal-to-noise ratio biomimetic in-situ aircraft surface turbulence mapping system. Nano Energy 2025;136:110694.

[32] Xu Z, Cao LNY, Li C, Luo Y, Su E, Wang W, et al. Digital mapping of surface turbulence status and aerodynamic stall on wings of a flying aircraft. Nat Commun 2023;14(1):2792.

[33] Gong Z, Di W, Jiang Y, Dong Z, Yang Z, Ye H, et al. Flexible calorimetric flow sensor with unprecedented sensitivity and directional resolution for multiple flight parameter detection. Nat Commun 2024;15(1):3091.

[34] Xiong W, Zhu C, Guo D, Hou C, Yang Z, Xu Z, et al. Bio-inspired, intelligent flexible sensing skin for multifunctional flying perception. Nano Energy 2021;90(Part A):106550.

[35] Yao Z, Wu W, Gao F, Gong M, Zhang L, Wang D, et al. Flexible tactile sensing systems: challenges in theoretical research transferring to practical applications. Nano-Micro Lett 2026;18(1):37.

[36] Chen M, An X, Zhao F, Chen P, Wang J, Zhang M, et al. Boosting sensitivity of cellulose pressure sensor via hierarchically porous structure. Nano-Micro Lett 2025;17(1):205.

[37] Chen Z, Qu C, Yao J, Zhang Y, Xu Y. Two-stage micropyramids enhanced flexible piezoresistive sensor for health monitoring and human-computer interaction. ACS Appl Mater Interfaces 2024;16(6):7640–9.

[38] Nie Z, Kwak JW, Han M, Rogers JA. Mechanically active materials and devices for bio-interfaced pressure sensors–a review. Adv Mater 2024;36(43):2205609.

[39] Xiong W, Zhang F, Qu S, Yin L, Li K, Huang Y. Marangoni-driven deterministic formation of softer, hollow microstructures for sensitivity-enhanced tactile system. Nat Commun 2024;15(1):5596.

[40] Ma Q, Liao S, Ma Y, Chu Y, Wang Y. An ultra-low-temperature elastomer with excellent mechanical performance and solvent resistance. Adv Mater 2021;33(36):2102096.

[41] Zhang X, Li D, Yang X, Wang L, Li G, Wong TW, et al. Hydro-locking in hydrogel for extreme temperature tolerance. Science 2025;387(6737):967–73.

[42] Zhu S, Peng S, Qiang Z, Ye C, Zhu M. Cryogenic-environment resistant, highly elastic hybrid carbon foams for pressure sensing and electromagnetic interference shielding. Carbon 2022;193:258–71.

[43] Zhao K, Zhang T, Chang H, Yang Y, Xiao P, Zhang H, et al. Super-elasticity of three-dimensionally cross-linked graphene materials all the way to deep cryogenic temperatures. Sci Adv 2019;5(4):eaav2589.

[44] Liu Q, Liu Y, Shi J, Liu Z, Wang Q, Guo CF. High-porosity foam-based iontronic pressure sensor with superhigh sensitivity of 9280 kPa^{-1}. Nano-Micro Lett 2022;14(1):21.

[45] He Y, Cheng Y, Yang C, Guo CF. Creep-free polyelectrolyte elastomer for drift-free iontronic sensing. Nat Mater 2024;23(8):1107–14.

[46] Bai N, Wang L, Wang Q, Deng J, Wang Y, Lu P, et al. Graded intrafillable architecture-based iontronic pressure sensor with ultra-broad-range high sensitivity. Nat Commun 2020;11(1):209.

[47] Chen D, Li J, Yuan Y, Gao C, Cui Y, Li S, et al. A review of the polymer for cryogenic application: methods, mechanisms and perspectives. Polymers 2021;13(3):320.

[48] Xie X, Jiang Y, Yao X, Zhang J, Zhang Z, Huang T, et al. A solvent-free processed low-temperature tolerant adhesive. Nat Commun 2024;15(1):5017.

[49] Sun P, Mei S, Xu JF, Zhang X. A bio-based supramolecular adhesive: ultra-high adhesion strengths at both ambient and cryogenic temperatures and excellent multi-reusability. Adv Sci 2022;9(28):2203182.

[50] Cheng Y, Zhang X, Qin Y, Dong P, Yao W, Matz J, et al. Super-elasticity at 4 K of covalently crosslinked polyimide aerogels with negative Poisson's ratio. Nat Commun 2021;12(1):4092.

[51] Yuan S, Bai J, Cao Y, Li S, Zhu H, Zhang T, et al. A high environmentally stable ionic hydrogel for pressure-temperature bimodal passive flexible tactile sensor. Adv Funct Mater 2026;36(3):e15806.

[52] Huang Y, Li Y, Peng C, Feng W. High-resilience, anti-freezing, and vacuum-tolerant eutectogel for self-powered pressure sensing in extreme environments. Sci China Mater 2026;69(1):460–72.

[53] Cheng M, Yuan Y, Li Q, Chen C, Chen J, Tian K, et al. Polyimide aerogel-based capacitive pressure sensor with enhanced sensitivity and temperature resistance. J Mater Sci Technol 2025;217:60–9.

[54] Li C, Xu R, Han D, Li P, Liu W, Guang M, et al. Gradient nanofiber aerogels for extreme cryogenic and thermal environments. Nat Commun 2026;17(1):721.

[55] Gao J, Zhao B, Chen X, Gu M, Zhang W, Wang L, et al. Harsh environment-tolerant, high performance soft pressure sensors enabled by fiber-segment structure and plasma treatment. Small 2024;20(49):2403495.

[56] Lototskaya VA, Yakovenko LF, Aleksenko EN, Abraimov VV, Shao WZ. Regularities of low-temperature deformation and fracture of polyimide films of kapton H type of different thickness. East Eur J Phys 2020;4:144–53.

[57] Liu J, Jiang S, Xiong W, Zhu C, Li K, Huang Y. Self-healing Kirigami assembly strategy for conformal electronics. Adv Funct Mater 2022;32(12):2109214.

[58] Xiao L, Zhu C, Xiong W, Huang Y, Yin Z. The conformal design of an island-bridge structure on a non-developable surface for stretchable electronics. Micromachines 2018;9(8):392.

[59] Chen Z, Guo Q, Majidi C, Chen W, Srolovitz DJ, Haataja MP. Nonlinear geometric effects in mechanical bistable morphing structures. Phys Rev Lett 2012;109(11):114302.

[60] Lai W, Di L, Zhao C, Tian Y, Duan Y, Pan Y, et al. Electrospray deposition for electronic thin films on 3D freeform surfaces: from mechanisms to applications. Adv Mater Technol 2024;9(22):2400192.

[61] Lu L, Leanza S, Zhao RR. Mechanical instabilities: from failure mechanism to functionality. Appl Mech Rev 2026;78(3):030801.

[62] Xiong W, Guo D, Yang Z, Zhu C, Huang Y. Conformable, programmable and step-linear sensor array for large-range wind pressure measurement on curved surface. Sci China Technol Sci 2020;63(10):2073–81.

[63] Lin P, Wu J, Lu L, Xiong N, Liu D, Su J, et al. Investigation on the reynolds number effect of a flying wing model with large sweep angle and small aspect ratio. Aerospace 2022;9(9):523.

[64] Lai H, Chen WH, Sun DW, Nie XT, Zhu CJ. The structural design for 0.3 m cryogenic continuous transonic wind tunnel. J Exp Fluid Mech 2020;34(5):89–96.

Declaration of interests

☒ The authors declare that they have no known competing financial interests or personal relationships that could have appeared to influence the work reported in this paper.